Scientific Reports

https://doi.org/10.1038/s41598-026-43617-2

Article in Press

# Nasal and oral breathing modes reconfigure brain network dynamics between stabilizing integration and promoting fragmentation

Received: 14 November 2025

Accepted: 5 March 2026

Published online: 03 April 2026

Cite this article as: Mohammadi S., Hossein-Zadeh G. & Raoufy M.R. Nasal and oral breathing modes reconfigure brain network dynamics between stabilizing integration and promoting fragmentation. *Sci Rep* (2026). https://doi.org/10.1038/s41598-026-43617-2

Sadeq Mohammadi, Gholam-Ali Hossein-Zadeh & Mohammad Reza Raoufy

# Nasal and oral breathing modes reconfigure brain network dynamics between stabilizing integration and promoting fragmentation

Sadeq Mohammadi[1], Gholam-Ali Hossein-Zadeh[1,2*], Mohammad Reza Raoufy[3,4]

1. Department of Bioelectric, School of Electrical and Computer Engineering, College of Engineering, University of Tehran, Tehran, Iran.

2. School of Cognitive Sciences, Institute for Research in Fundamental Sciences (IPM), Tehran, Iran.

3. Department of Physiology, Faculty of Medical Sciences, Tarbiat Modares University, Tehran, Iran.

4. Institute for Brain Sciences and Cognition, Tarbiat Modares University, Tehran, Iran.

* Correspondence: Gholam-Ali Hossein-Zadeh (ghzadeh@ut.ac.ir)

Department of Bioelectric,

School of Electrical and Computer Engineering,

College of Engineering,

University of Tehran,

Tehran, Iran.

# Abstract

Breathing rhythmically coordinates neural oscillations across the brain, yet how the breathing mode (nasal vs. oral) modulates large-scale functional networks over time remains unclear. Building on prior static connectivity findings, this study applied dynamic functional connectivity (dFC) analysis using a Hidden Markov Model (HMM) to resting-state fMRI data from 20 healthy adults during nasal and oral breathing, focusing on the 0.1–0.2 Hz frequency band. Three recurrent brain states were identified: (1) a weakly connected, segregated state; (2) a globally integrated state dominated by default mode, frontoparietal, salience, and limbic networks; and (3) a partially segregated intermediate state. Compared with oral breathing, nasal breathing stabilized the integrated state, increasing its lifetime (p-FDR = 0.03) and reducing switching rates (p-FDR = 0.002). Oral breathing showed greater fractional occupancy of the intermediate state (p-FDR = 0.03) and a higher probability of transitions from integration to fragmentation (p-FDR = 0.02). Graph-theoretic analysis also revealed that nasal breathing supported the configuration with higher efficiency and lower modularity. Taken together, this study provides the first respiration-entrained, HMM-based dFC analysis of resting-state fMRI, demonstrating that nasal breathing entrains a stable, globally coherent state, whereas oral breathing disrupts this stability and promotes fragmented network organization.





## Keywords

Breathing, Brain function, Brain networks, Resting-state fMRI, Dynamic functional connectivity, Hidden Markov model

# Introduction

Beyond its survival role, breathing is a fundamental rhythm that can entrain neural oscillations across widespread brain regions and modulate cognitive and emotional processes[1-4]. Nasal breathing provides direct mechanosensory input via olfactory sensory neurons (OSNs), which stimulate the olfactory bulb and propagate rhythmic signals to cortical and limbic regions[5,6]. By contrast, oral breathing bypasses this sensory input, leaving brainstem central pattern generators as the primary oscillatory drivers of brain–body coordination[7-9]. These dual pathways suggest that breathing mode (nasal vs. oral) differentially modulates large-scale brain organization, with implications for interoception, emotion regulation, and cognition[1,2,5,7,10,11].

Building on this premise, our recent resting-state fMRI study demonstrated that breathing mode selectively modulates functional brain connectivity within the intermediate frequency band of 0.1–0.2 Hz[11], consistent with the brain's binary hierarchical model of frequency architecture[12]. Specifically, nasal breathing preferentially engages cortical regions through the olfactory pathway, whereas oral breathing enhances subcortical connectivity, leading us to propose the respiration-entrained brain oscillation network (REBON)[11]. However, this prior work was fundamentally static, whereas converging evidence indicates that large-scale brain networks reconfigure dynamically on timescales of seconds to minutes[13,14]. Thus, it remains unknown how breathing mode reorganizes large-scale network dynamics over time. A key unanswered question is therefore which dynamic states are stabilized or destabilized by nasal versus oral breathing, and how these shifts influence the topological balance between large-scale integration and segregation.

Capturing this temporal flexibility is critical for understanding respiration-entrained neural activity, which is inherently rhythmic and state-dependent. Dynamic functional connectivity (dFC) provides a framework for identifying recurring brain states and characterizing their temporal properties[13,14]. Although the sliding-window method has been widely used, it is limited by arbitrary parameter choices and susceptibility to noise[15,16]. The Hidden Markov Model (HMM) offers a powerful alternative, providing a probabilistic and data-driven framework for directly inferring brain states from the BOLD signal without predefined window lengths[17,18]. Applications of the HMM in cognitive and clinical neuroscience have demonstrated its capacity to reveal latent brain dynamics that remain invisible to static analyses[19-21].

Recent works have highlighted the frequency-specific organization of resting-state BOLD signals beyond the conventional low-frequency band (0.01–~0.09 Hz)[22]. In this study, we focused on the intermediate band of 0.1–0.2 Hz (centered around ~0.16 Hz), based on the binary hierarchy model[12]. Empirical

fMRI studies indicate that this frequency range captures respiration-entrained BOLD fluctuations and supports neural synchrony driven by respiration-locked oscillations that organize large-scale functional connectivity[11]. Accordingly, we ensured that our analyses isolated respiration-driven neural synchronization rather than broadband or nonspecific noise.

This work directly addresses the open question of how breathing mode dynamically reconfigures resting-state brain networks. Using an HMM-based dynamic functional connectivity approach, we characterized recurrent connectivity states and their temporal properties (fractional occupancy, lifetime, switching rate, and transition probabilities) under nasal versus oral breathing conditions. To our knowledge, this is the first respiration-entrained resting-state fMRI evidence demonstrating that breathing mode reorganizes large-scale functional connectivity, offering new insights into the temporal coupling of brain networks and potential implications for cognitive enhancement and neurorehabilitation.

# Methods

All data acquisition and preprocessing procedures were identical to our recent study[11]. To avoid redundancy, we provide a brief overview of participant characteristics, data acquisition, and preprocessing and denoising, while focusing on ROI and network definition and the implementation of dFC analysis using an HMM framework. A schematic overview of the complete analysis workflow is shown in Fig. 1.

## Participants

Twenty-five healthy, right-handed adult males (mean ± SD = 23.9 ± 2.2 years) participated in this study. None had a history of neurological, psychiatric, respiratory, or cardiovascular disorders; traumatic brain injury; respiratory or nasal conditions; prior COVID-19 infection; smoking or substance use; claustrophobia; or metal implants. All participants achieved normal scores on the General Health Questionnaire-28 (GHQ-28)[23,24] and the Depression Anxiety Stress Scales-42[25,26]. Participants showing structural abnormalities on T1-weighted MRI or excessive head motion during scanning (2 mm displacement or 2 degrees of rotation) were excluded. After applying motion, quality-control, and outlier criteria, the final sample comprised 20 participants.

All participants reviewed and signed a written informed consent form and were not informed of the study's aims to maintain blinding. The study protocol was approved by the Ethics Committee of Tarbiat Modares University (IR.MODARES.REC.1400.175). All methods were performed in accordance with

relevant guidelines and regulations, including the Declaration of Helsinki. No identifiable participant information or images were included in the manuscript.

## Data acquisition

Data were collected at the National Brain Mapping Lab, Tehran, Iran, using a 3-Tesla Siemens Prisma scanner equipped with a 20-channel head coil. Structural images were obtained with a T1-weighted MPRAGE sequence (TR = 2000 ms, TE = 3.47 ms, flip angle = 7°, voxel size = 1 × 1 × 1 $mm^3$). Resting-state functional MRI data were acquired with a T2*-weighted gradient-echo EPI sequence (TR = 2000 ms, TE = 30 ms, flip angle = 90°, voxel size = 3 × 3 × 4 $mm^3$).

Each participant underwent a single resting-state fMRI session that included two 10-minute runs, nasal breathing and oral breathing, in a randomized order. Nasal breathing adherence was enforced through the use of mouth tape, and oral breathing was confirmed using a soft silicone nose clip. To reduce carryover effects and allow for physiological recovery, an interval of approximately 15 minutes was maintained between runs. Before each 10-minute resting-state fMRI scan, participants spent five minutes breathing in the same assigned mode (nasal or oral) to stabilize respiratory patterns. ECG and respiration were monitored and recorded with the Physiological Monitoring Unit (PMU Wireless Physio Control, Siemens, Erlangen, Germany) to ensure a natural heart rate (HR) and breathing pattern. Throughout scanning, participants were instructed to keep their eyes open and fixate on a central crosshair displayed on a dark background.

## Preprocessing and denoising

Data preprocessing was performed using fMRIPrep 20.2.6 (Nipype 1.7.0)[27-30]. In summary, preprocessing included removal of the first five volumes (leaving 295 volumes), motion correction[31], slice-timing correction[32], fieldmap-based distortion correction[33], co-registration of BOLD to T1-weighted images[34,35], and normalization to 2 mm MNI152 space[36]. Smoothing and denoising were carried out using CONN[37,38] (SPM12[39] dependency), with an 8 mm FWHM Gaussian kernel, regression of six head-motion parameters, linear detrending, and band-pass filtering between 0.1 and 0.2 Hz.

## ROI and network definition

Preprocessed BOLD time series were extracted using 116 ROIs defined by the AAL atlas[40]. To align with our recent study[11], the right and left olfactory regions were merged into a single olfactory ROI. Following Qiu et al.[41], ROIs were grouped into nine functional networks: seven cortical networks described by Yeo et al.[42] (VN: Visual Network (14 ROIs), SMN: Sensorimotor Network (14 ROIs), DAN: Dorsal Attention Network (2 ROIs), SN: Salience Network (6 ROIs),

LN: Limbic Network (11 ROIs), FPN: Frontoparietal Network (14 ROIs), DMN: Default Mode Network (16 ROIs)), a subcortical network (12 ROIs) defined by Tian et al.[43], and 26 cerebellar ROIs (CN). Finally, the brainstem region was added from the Harvard-Oxford atlas[44] to ensure full brain coverage. A complete list of ROIs and their network assignments is provided in Supplementary Table 1. Figure 1a illustrates a schematic overview of the analysis pipeline from data acquisition to ROI time course extraction.

This study aims to compare the effects of nasal versus oral breathing on whole-brain dynamic functional connectivity. Prior work has shown that breathing-mode effects prominently involve anatomically defined limbic, subcortical, and brainstem regions central to respiration–brain coupling within the REBON framework[11], many of which are not included in cortical functional parcellations such as the Schaefer (2018) atlas[45]. To ensure full coverage of regions critical to this objective, we therefore adopted the AAL116 atlas for whole-brain dynamic connectivity analysis.

## Dynamic functional connectivity analysis

Dynamic functional connectivity was estimated using a Hidden Markov Model (HMM) implemented in the HMM-MAR toolbox (https://github.com/OHBA-analysis/HMM-MAR) in MATLAB (The MathWorks Inc., USA). The HMM is an unsupervised probabilistic framework that models brain activity as a finite set of recurrent functional states, each characterized by distinct patterns of regional interactions[19]. Each state is represented as a multivariate Gaussian distribution, with the mean vector capturing average regional activity and the covariance matrix reflecting the corresponding functional connectivity pattern[17]. This formulation enables the HMM to capture both regional co-activation and the temporal reconfiguration of these interactions.

Model estimation was performed using variational Bayes inference, which iteratively minimizes free energy to achieve optimal model fitting[13,17]. The HMM yields two principal outputs: (1) state-specific parameters (means and covariance matrices) that define the functional architecture of each state, and (2) a state time course derived from posterior probabilities of state occupancy at each time frame. For each frame, the state with the highest posterior probability is assigned as the active state, resulting in a temporal sequence of recurring network configurations[18].

For implementation, the preprocessed ROI time series were concatenated across subjects into an input matrix of 11,800 × 116 for the HMM (11,800 volumes: 40 runs × 295 volumes; 116 ROIs). Because such high-dimensional data can easily lead to overfitting, dimensionality was reduced using the HMM-MAR PCA option, retaining 80% of signal variance (options.pca = 0.8). This step mitigated overfitting[20] and improved the reproducibility and stability of

the detected brain states. Figure 1b provides a simplified schematic of the HMM analysis pipeline.

To select the optimal number of HMM states, zero-mean Gaussian observation models were estimated with state numbers ranging from 2 to 8, with each model run 100 times to ensure robustness. The number of states was determined based on minimum free energy, which provides a critical measure of model stability[17], and median fractional occupancy, which serves as an index of state mixing[20]. Following prior work in dynamic functional connectivity research[46], we required that all states exhibit a median fractional occupancy greater than 0.1. This threshold ensures that selected states reflect reliable and well-separated dynamics rather than spurious or poorly mixed states[47].

For each state, the model yielded a covariance matrix representing functional connectivity, while group differences were examined in the temporal properties of state dynamics derived from the state time course. Specifically, we assessed three metrics: (1) fractional occupancy, the fraction of scanning time occupied by a given state[17]; (2) lifetime, the average consecutive duration within a state[41]; and (3) switching rate, the number of transitions between states per unit time[19]. In addition, transition probability matrices (TPMs) were estimated separately for each breathing condition[47]. Group differences were tested using paired permutation tests (100,000 iterations) with FDR correction[48].

Topological differences were assessed using the Brain Connectivity Toolbox (https://sites.google.com/site/bctnet)[49]. We constructed weighted undirected graphs of each state by retaining the top 1–50% of positive functional connections and then compared three network measures: (1) global efficiency, the mean of the inverse shortest path lengths between all pairs of nodes, representing the network's overall capacity for integrated communication[50]; (2) local efficiency, the global efficiency computed within the immediate neighborhood of each node, reflecting the network's capacity for specialized and robust communication[50]; and (3) modularity, a measure that quantifies the degree to which the network is segregated into distinct subnetworks (modules)[51]. Figure 1c summarizes the dynamic state characterization.

# Results

## Optimal HMM model

Supplementary Fig. 1 shows the average minimum free energy across models with 2–8 states. Free energy decreased monotonically with increasing state

numbers, without a clear local minimum or elbow point[14] to guide model selection. Therefore, fractional occupancy was used as the main criterion. Supplementary Fig. 2 depicts fractional occupancy values across different state numbers. Beginning with the four-state solution, at least one state consistently exhibited fractional occupancy < 0.1. Based on this criterion, we selected the three-state HMM with the lowest free energy as the optimal model.

## Functional connectivity of brain states

The HMM analysis identified three recurrent brain states, each characterized by distinct patterns of functional connectivity across large-scale networks (Fig. 2). To improve visualization, representative graphs of each state (showing edges with correlation > 0.8) are displayed below the corresponding connectivity matrices, generated using BrainNet Viewer (http://www.nitrc.org/projects/bnv/)[52]. Across all concatenated data (both breathing conditions), the three HMM states exhibited fractional occupancies of 28.5%, 43.5%, and 28.0%, respectively. State 1 (Fig. 2a) exhibited relatively weak global connectivity, dominated by within-network links and markedly reduced inter-network interactions. The graph highlights a sparsely connected configuration with limited cross-network integration. State 2 (Fig. 2b) represented the most dominant and integrated state, characterized by widespread positive correlations both within and across networks. Notably, dense coupling was observed among higher-order systems, including the SN, FPN, and DMN. The corresponding graph shows a highly interconnected architecture consistent with a globally integrated configuration. State 3 (Fig. 2c) displayed a partially segregated profile, characterized by moderate connectivity that was stronger within specific networks, including VN, SMN, and SN, and by selective clusters of inter-network coupling. This pattern contrasted with the more extensive integration of state 2, as reflected in the graph representation of an intermediate configuration.

## Temporal dynamics measures

Figure 3 illustrates the comparison of temporal dynamics across the three identified states during nasal and oral breathing. Condition-specific fractional occupancies, computed separately for nasal and oral breathing runs (Fig. 3a) and statistically compared, revealed a significant effect of breathing condition in state 3, with higher occupancy observed during oral breathing than nasal breathing (FDR-corrected $p = 0.031$). Lifetime analysis (Fig. 3b) indicated that state 2 persisted significantly longer during nasal breathing (p-FDR = 0.034). Finally, the switching rate (Fig. 3c) was significantly higher during oral compared to nasal breathing (p-FDR = 0.002).

### State transition probabilities

The results of the state transition probabilities are shown in Figs. 4 and 5. The difference matrix of mean transition probabilities between nasal and oral breathing (Fig. 4a) revealed the most prominent effect in transitions from state 2 to state 3, which were significantly more frequent during oral breathing. This effect was confirmed by statistical testing (Fig. 4b), with a significant difference (p-FDR = 0.022). No other transitions showed significant differences between conditions.

Figure 5 provides directed graphs of Markov transition probabilities, excluding self-transitions to emphasize cross-state changes. Under nasal breathing, transitions were relatively balanced, with a greater tendency toward state 2 (Fig. 5a). By contrast, oral breathing exhibited a pronounced directional bias from state 2 to state 3, together with an elevated bidirectional exchange between these two states (Fig. 5b).

### Connectivity topology across states

Graph-theoretic properties of each state are shown in Fig. 6. Global efficiency (Fig. 6a) was highest in state 2 across a wide range of connection densities, followed by state 3 and then state 1. Local efficiency (Fig. 6b), averaged across 116 ROIs, exhibited the same ordering across states. In contrast, modularity (Fig. 6c) was lowest in state 2, whereas states 1 and 3 consistently exhibited higher modularity across all thresholds.



## Discussion

This study demonstrates that the mode of breathing modulates the dynamic organization of large-scale brain networks. Using an HMM applied to resting-state fMRI, we identified three recurrent connectivity states that varied from segregated to globally integrated configurations. State 1 showed overall weak correlations and a highly modular pattern dominated by local interactions, likely reflecting a low-demand baseline in which large-scale coordination is minimized. State 2 emerged as the most dominant state, characterized by widespread increases in connectivity across the DMN, FPN, SN, and LN, alongside enhanced coupling with subcortical structures including the hippocampus, thalamus, and amygdala. This architecture is consistent with nasal respiration entraining limbic–cognitive circuits[5,8,9,11]. State 3 represented an intermediate configuration, preserving within-network coherence in the VN, SMN, and SN, but network coupling, particularly between the DMN, FPN, LN, and subcortical regions, was attenuated relative to state 2.

Breathing mode strongly influenced the temporal dynamics of these states. Nasal breathing stabilized the integrated state 2, prolonging its lifetime and reducing transitions away from it, whereas oral breathing promoted greater occupancy of the partially segregated state 3 and increased switching rates. This divergence reflects a fundamental contrast in how the two modes influence large-scale coordination: nasal respiration maintains globally coherent dynamics, whereas oral respiration fragments them. Transition probabilities further highlighted this contrast, as oral breathing increased the likelihood of leaving the integrated state 2 for the fragmented state 3, while nasal breathing reduced such transitions and preserved global coherence.

These effects can be traced to the sensory pathways engaged by nasal breathing and bypassed by oral breathing. Nasal breathing stimulates OSNs, which act as both odor detectors and mechanical sensors[6]. Rhythmic OSN activation drives oscillatory activity in the olfactory bulb and propagates to limbic and cortical regions[5,8], entraining widespread oscillations, particularly in the gamma range[53]. This reafferent input, driven by respiration via the olfactory bulb[7], reinforces global coherence and promotes temporally stable network states. In contrast, oral breathing bypasses OSN stimulation and relies primarily on brainstem respiratory pacemakers such as the preBötzinger complex[54]. While sufficient for rhythmicity and homeostatic control, these pacemakers lack the cortical–limbic entrainment afforded by nasal airflow[3,4,11]. As a result, oral breathing destabilizes the balance between integration and segregation, leading to shorter lifetimes of the integrated state and higher switching rates. This interpretation aligns with electrophysiological studies showing that nasal breathing entrains cortical oscillations, whereas oral breathing abolishes such effects[5,55].

Graph-theoretic analyses further supported these observations. State 2, which predominated during nasal breathing, exhibited high global and local efficiency and low modularity, reflecting an architecture optimized for information exchange and flexible cognition. In contrast, state 3, more prominent during oral breathing, showed lower efficiency and higher modularity, indicating a segregated, locally specialized configuration. State 1 displayed the weakest efficiency and highest modularity, consistent with a disengaged baseline state. These findings parallel prior dynamic connectivity studies, indicating that integrated states support long-range coordination, whereas segregated states constrain processing to within-network loops[56]. Consistent with these patterns, an EEG study in mechanically ventilated comatose patients demonstrated that rhythmic nasal air-puff stimulation increased both global and local efficiencies across the default mode network and enhanced gamma-band connectivity, indicating improved network integration[57]. A complementary EEG study in healthy subjects likewise showed

that nasal breathing or nasal air-puffing increased power within DMN nodes, particularly in frontal regions, in the gamma frequency range and enhanced cortical synchrony relative to oral breathing[55].

The stabilization of the integrated state during nasal breathing has important cognitive implications. This configuration links the DMN, FPN, SN, LN, and subcortical regions, supporting key functions including memory, attention, emotional regulation, and conscious processing[2,58,59]. By promoting the persistence of such configurations, nasal breathing may facilitate cognitive flexibility and long-range communication. Conversely, oral breathing biases the system toward fragmented states, aligning with evidence that mouth breathing is associated with impaired attention, weaker executive control, and memory deficits[60,61]. Nasal airflow provides an external driver that couples limbic and cortical oscillations[7,11], whereas oral breathing deprives the system of this synchronizing input, limiting access to higher-order circuits. This mechanistic distinction may explain why nasal breathing enhances cognitive and emotional processing[5,9], while chronic oral breathing is associated with cognitive impairments[61].

These findings also have translational implications. Interventions that stimulate OSNs, such as controlled nasal breathing exercises (e.g., meditation practices[58]), rhythmic air-puff stimulation[55], or electrical activation of the epithelium[62], may reinforce stable, integrated brain states and could help mitigate memory decline[63] or slow the progression of Alzheimer's disease[64]. Recent evidence further highlights the olfactory bulb as a promising target for deep brain stimulation, as electrical stimulation of this region has been shown to reduce seizure severity and restore memory in kindled rats[65], as well as to alleviate depressive-like behaviors and improve prefrontal–hippocampal coherence[66]. Such approaches may offer a noninvasive pathway for enhancing higher-order brain function; however, clinical trials are needed to evaluate their feasibility, safety, and efficacy.

Despite the insights gained, several limitations warrant consideration. The relatively small and demographically homogeneous sample limits generalizability. Larger and more diverse samples will be required to confirm the robustness of these findings. The exclusive use of resting-state fMRI without concurrent behavioral assessments constrains functional interpretation. Future studies should incorporate cognitive tasks or behavioral measures to directly link breathing-related dynamics with cognition. Another challenge concerns the determination of the optimal number of states. While using a larger state space can capture finer temporal detail[13,19], it also raises the risk of poor state mixing and identifying spurious or subject-specific states[41,46,47]. In this study, we prioritized a balance between sufficient complexity, stable mixing, and minimizing spurious dynamics. Nevertheless,

the absence of a consensus on methods for selecting the optimal number of states remains an open methodological issue. Finally, although we demonstrated in our previous study[11] using the same dataset that potential physiological and autonomic confounds, including heart rate variability (HRV), respiratory volume per time (RVT), and aliasing effects, were ruled out as significant confounds, others factors such as arousal, fatigue, and blood gas exchange may still contribute and should be directly measured in future work.

# Conclusion

This study provides the first respiration-entrained, frequency-specific HMM-based dFC analysis of resting-state fMRI data comparing different breathing modes. Our results reveal a globally integrated brain state that is stabilized by nasal breathing, characterized by longer lifetimes and reduced switching rates. This state links higher-order cortical and limbic systems, facilitating between-network coordination, as reflected in higher global and local efficiency and lower modularity. In contrast, oral breathing promotes a more fragmented and less stable configuration, with greater fractional occupancy, higher switching rates, and a directional bias from integration toward partial fragmentation. These findings connect OSN-driven reafference with the stability of integrated network states, suggesting that the rhythmic entrainment provided by nasal airflow is crucial for sustaining brain-wide coherence and may underlie the behavioral advantages of nasal breathing in cognition and emotion. Together, these results elevate breathing mode from a peripheral physiological factor to a potential mechanism for network-level control, carrying translational implications for cognitive enhancement and clinical intervention.



# References


1 Tort, A. B., Laplagne, D. A., Draguhn, A. & Gonzalez, J. Global coordination of brain activity by the breathing cycle. *Nat Rev Neurosci*, 1-21 (2025).

2 Heck, D. H. *et al.* Recent insights into respiratory modulation of brain activity offer new perspectives on cognition and emotion. *Biol. Psychol.* **170**, 108316 (2022).

3 Tort, A. B., Brankačk, J. & Draguhn, A. Respiration-entrained brain rhythms are global but often overlooked. *Trends Neurosci.* **41**, 186-197 (2018).

4 Heck, D. H. *et al.* Breathing as a fundamental rhythm of brain function. *Front Neural Circuits* **10**, 115 (2017).

5 Zelano, C. *et al.* Nasal respiration entrains human limbic oscillations and modulates cognitive function. *J. Neurosci.* **36**, 12448-12467 (2016).

6 Grosmaitre, X., Santarelli, L. C., Tan, J., Luo, M. & Ma, M. Dual functions of mammalian olfactory sensory neurons as odor detectors and mechanical sensors. *Nat. Neurosci.* **10**, 348-354 (2007).

7 Karalis, N. & Sirota, A. Breathing coordinates cortico-hippocampal dynamics in mice during offline states. *Nature communications* **13**, 467 (2022).

8 Folschweiller, S. & Sauer, J.-F. Respiration-Driven Brain Oscillations in Emotional Cognition. *Front Neural Circuits* **15**, 761812 (2021).

9 Herrero, J. L., Khuvis, S., Yeagle, E., Cerf, M. & Mehta, A. D. Breathing above the brain stem: volitional control and attentional modulation in humans. *J. Neurophysiol.* (2018).

10 Goheen, J., Anderson, J. A., Zhang, J. & Northoff, G. From lung to brain: respiration modulates neural and mental activity. *Neurosci. Bull.* **39**, 1577-1590 (2023).

11 Mohammadi, S., Hossein-Zadeh, G.-A. & Raoufy, M. R. Breathing mode selectively modulates brain-wide functional connectivity. *PLoS One* **20**, e0334165 (2025).

12 Klimesch, W. The frequency architecture of brain and brain body oscillations: an analysis. *Eur. J. Neurosci.* **48**, 2431-2453 (2018).

13 Vidaurre, D., Smith, S. M. & Woolrich, M. W. Brain network dynamics are hierarchically organized in time. *Proceedings of the National Academy of Sciences* **114**, 12827-12832 (2017).

14 Allen, E. A. *et al.* Tracking whole-brain connectivity dynamics in the resting state. *Cereb. Cortex* **24**, 663-676 (2014).

15 Lurie, D. J. *et al.* Questions and controversies in the study of time-varying functional connectivity in resting fMRI. *Network neuroscience* **4**, 30-69 (2020).

16 Hutchison, R. M. *et al.* Dynamic functional connectivity: promise, issues, and interpretations. *Neuroimage* **80**, 360-378 (2013).

17 Vidaurre, D. *et al.* Spectrally resolved fast transient brain states in electrophysiological data. *Neuroimage* **126**, 81-95 (2016).

18 Baker, A. P. *et al.* Fast transient networks in spontaneous human brain activity. *elife* **3**, e01867 (2014).

19 Geng, L. *et al.* Depression links to unstable resting-state brain dynamics: insights from hidden markov models and functional network variability. *Psychol. Med.* **55**, e200 (2025).

20 Zhang, X. *et al.* Reconfiguration of brain network dynamics in bipolar disorder: a hidden Markov model approach. *Translational Psychiatry* **14**, 507 (2024).

21 Kottaram, A. *et al.* Brain network dynamics in schizophrenia: Reduced dynamism of the default mode network. *Hum. Brain Mapp.* **40**, 2212-2228 (2019).

22 Zheng, X. *et al.* Frequency-specific alterations of the resting-state BOLD signals in nocturnal enuresis: an fMRI Study. *Sci. Rep.* **11**, 12042 (2021).

23 Sterling, M. General health questionnaire–28 (GHQ-28). *J. Physiother.* **57**, 259 (2011).

24 Goldberg, D. P. & Hillier, V. F. A scaled version of the General Health Questionnaire. *Psychol. Med.* **9**, 139-145 (1979).

25 Parkitny, L. & McAuley, J. The depression anxiety stress scale (DASS). *J. Physiother.* **56**, 204 (2010).

26 Lovibond, P. F. & Lovibond, S. H. The structure of negative emotional states: Comparison of the Depression Anxiety Stress Scales (DASS) with the Beck Depression and Anxiety Inventories. *Behav. Res. Ther.* **33**, 335-343 (1995).

27 Esteban, O. *et al.* fMRIPrep: a robust preprocessing pipeline for functional MRI. *Nat Methods* **16**, 111-116 (2019).

28 Gorgolewski, K. J. *et al.* Nipype. *Zenodo* (2018). https://doi.org/10.5281/zenodo.596855.

29 Esteban, O. *et al.* fMRIPrep. *Zenodo* (2018). https://doi.org/10.5281/zenodo.852659

30 Gorgolewski, K. *et al.* Nipype: a flexible, lightweight and extensible neuroimaging data processing framework in python. *Front. Neuroinform.* **5**, 13 (2011).

31 Jenkinson, M., Bannister, P., Brady, M. & Smith, S. Improved optimization for the robust and accurate linear registration and motion correction of brain images. *Neuroimage* **17**, 825-841 (2002).

32 Cox, R. W. & Hyde, J. S. Software tools for analysis and visualization of fMRI data. *NMR in Biomedicine: An International Journal Devoted to the Development and Application of Magnetic Resonance In Vivo* **10**, 171-178 (1997).

33 Glasser, M. F. *et al.* The minimal preprocessing pipelines for the Human Connectome Project. *Neuroimage* **80**, 105-124 (2013).

34 Dale, A. M., Fischl, B. & Sereno, M. I. Cortical surface-based analysis: I. Segmentation and surface reconstruction. *Neuroimage* **9**, 179-194 (1999).

35 Greve, D. N. & Fischl, B. Accurate and robust brain image alignment using boundary-based registration. *Neuroimage* **48**, 63-72 (2009).

36 Avants, B. B., Epstein, C. L., Grossman, M. & Gee, J. C. Symmetric diffeomorphic image registration with cross-correlation: evaluating automated labeling of elderly and neurodegenerative brain. *Med. Image Anal.* **12**, 26-41 (2008).

37 Nieto-Castanon, A. & Whitfield-Gabrieli, S. CONN functional connectivity toolbox: RRID SCR_009550, release 22. (2022).

38 Whitfield-Gabrieli, S. & Nieto-Castanon, A. Conn: a functional connectivity toolbox for correlated and anticorrelated brain networks. *Brain Connect.* **2**, 125-141 (2012).

39 Penny, W. D., Friston, K. J., Ashburner, J. T., Kiebel, S. J. & Nichols, T. E. *Statistical parametric mapping: the analysis of functional brain images*. (Elsevier, 2011).

40 Tzourio-Mazoyer, N. *et al.* Automated anatomical labeling of activations in SPM using a macroscopic anatomical parcellation of the MNI MRI single-subject brain. *Neuroimage* **15**, 273-289 (2002).

41 Qiu, Z. *et al.* Altered brain dynamics in chronic neck and shoulder pain revealed by hidden Markov model. *Sci. Rep.* **15**, 18018 (2025).

42 Yeo, B. T. *et al.* The organization of the human cerebral cortex estimated by intrinsic functional connectivity. *J. Neurophysiol.* (2011).

43 Tian, Y., Margulies, D. S., Breakspear, M. & Zalesky, A. Topographic organization of the human subcortex unveiled with functional connectivity gradients. *Nat. Neurosci.* **23**, 1421-1432 (2020).

44 Desikan, R. S. *et al.* An automated labeling system for subdividing the human cerebral cortex on MRI scans into gyral based regions of interest. *Neuroimage* **31**, 968-980 (2006).

45 Schaefer, A. *et al.* Local-global parcellation of the human cerebral cortex from intrinsic functional connectivity MRI. *Cereb. Cortex* **28**, 3095-3114 (2018).

46 Bonkhoff, A. K. *et al.* Acute ischaemic stroke alters the brain's preference for distinct dynamic connectivity states. *Brain* **143**, 1525-1540 (2020).

47 Vidaurre, D. *et al.* Discovering dynamic brain networks from big data in rest and task. *Neuroimage* **180**, 646-656 (2018).

48 Benjamini, Y. & Hochberg, Y. Controlling the false discovery rate: a practical and powerful approach to multiple testing. *J R Stat Soc Series B Stat Methodol* **57**, 289-300 (1995).

49 Rubinov, M. & Sporns, O. Complex network measures of brain connectivity: uses and interpretations. *Neuroimage* **52**, 1059-1069 (2010).

50 Latora, V. & Marchiori, M. Efficient behavior of small-world networks. *Phys. Rev. Lett.* **87**, 198701 (2001).

51 Newman, M. E. Modularity and community structure in networks. *Proceedings of the national academy of sciences* **103**, 8577-8582 (2006).

52 Xia, M., Wang, J. & He, Y. BrainNet Viewer: a network visualization tool for human brain connectomics. *PLoS One* **8**, e68910 (2013).

53 González, J. *et al.* Breathing modulates gamma synchronization across species. *Pflugers Arch* **475**, 49-63 (2023).

54 Del Negro, C. A., Funk, G. D. & Feldman, J. L. Breathing matters. *Nat Rev Neurosci* **19**, 351-367 (2018).

55 Salimi, M. *et al.* Nasal airflow promotes default mode network activity. *Respir. Physiol. Neurobiol.* **307**, 103981 (2023).

56 Shine, J. M. *et al.* The dynamics of functional brain networks: integrated network states during cognitive task performance. *Neuron* **92**, 544-554 (2016).

57 Salimi, M. *et al.* Nasal air puff promotes default mode network activity in mechanically ventilated comatose patients: a noninvasive brain stimulation approach. *Neuromodulation* **25**, 1351-1363 (2022).
58 Zaccaro, A., Piarulli, A., Melosini, L., Menicucci, D. & Gemignani, A. Neural correlates of non-ordinary states of consciousness in pranayama practitioners: the role of slow nasal breathing. *Front. Syst. Neurosci.* **16**, 803904 (2022).
59 Zhou, G. *et al.* Human hippocampal connectivity is stronger in olfaction than other sensory systems. *Prog. Neurobiol.* **201**, 102027 (2021).
60 Bayrak, Ö., Polastri, M. & Pehlivan, E. Effects of Nasal and Oral Breathing on Respiratory Muscle and Brain Function: A Review. *Thoracic Research and Practice* **26**, 145 (2025).
61 Kuroishi, R. C. S., Garcia, R. B., Valera, F. C. P., Anselmo-Lima, W. T. & Fukuda, M. T. H. Deficits in working memory, reading comprehension and arithmetic skills in children with mouth breathing syndrome: analytical cross-sectional study. *Sao Paulo Med. J.* **133**, 78-83 (2014).
62 Ghazvineh, S., Mooziri, M., Salimi, A., Mirnajafi-Zadeh, J. & Raoufy, M. R. Olfactory epithelium electrical stimulation mitigates memory and synaptic deficits caused by mechanical ventilation. *Sci. Rep.* **15**, 12197 (2025).
63 Ghazvineh, S. *et al.* Rhythmic air-puff into nasal cavity modulates activity across multiple brain areas: A non-invasive brain stimulation method to reduce ventilator-induced memory impairment. *Respir. Physiol. Neurobiol.* **287**, 103627 (2021).
64 Salimi, M. *et al.* Olfactory bulb stimulation mitigates Alzheimer's-like disease progression. *CNS Neurosci. Ther.* **30**, e70056 (2024).
65 Khodadadi, M. *et al.* Effect of low frequency stimulation of olfactory bulb on seizure severity, learning, and memory in kindled rats. *Epilepsy Res.* **188**, 107055 (2022).
66 Bastani, M. *et al.* Deep brain stimulation of the olfactory bulb alleviates depressive-like behaviors and alters prefrontal cortex hippocampal coherence. *Brain Res.*, 149902 (2025).

# Acknowledgements

The authors would like to acknowledge NBML for providing data acquisition facilities.

# Author contributions

MR.R. conceptualized the study. S.M. and GA.HZ. designed the study. S.M. performed the experiments, analyzed the data, and drafted the manuscript.

GA.HZ. supervised the study. All authors discussed and interpreted the results, reviewed the manuscript, and approved the final version.

## Data availability

Data are available from the corresponding author upon reasonable request.

## Competing interests

The authors declare no competing interests.

## Funding

This study received no funding.

## Figure Legends

**Fig. 1. Schematic overview of the analysis pipeline.** (a) Data acquisition, preprocessing, and ROI time course extraction: Resting-state fMRI data were collected during nasal and oral breathing conditions. Preprocessing and denoising were performed using fMRIPrep and CONN, after which regional time courses were extracted from the brain template. (b) Hidden Markov Model (HMM) analysis: ROI time courses were first reduced via principal component analysis (PCA) and then used as HMM input. The HMM estimated the most probable temporal sequence of recurrent brain states, each modeled as a Gaussian observation distribution. (c) Dynamic-state characterization: For each state, we quantified functional connectivity, connectivity topology (global efficiency, local efficiency, modularity), temporal dynamics (fractional occupancy, lifetime, switching rate), and transition probabilities.

**Fig. 2. Functional connectivity matrices of brain states (top panels) and corresponding graph representations with edges thresholded at correlation > 0.8 (lower panels).** (a) State 1 (28.5%) reflects a weakly connected, segregated configuration with reduced between-network coupling. (b) State 2 (43.5%) represents a globally integrated pattern with strong between-network coupling. (c) State 3 (28.0%) shows an intermediate profile with localized within-network coherence and attenuated between-network coupling. Connectivity matrices were generated using MATLAB (The

MathWorks Inc., USA). The lower panels depict graph-based visualizations of the corresponding connectivity patterns overlaid on a glass-brain rendering generating using BrainNet Viewer. Nodes represent ROIs and are color-coded by network affiliation, and edges indicate positive functional connections exceeding the correlation > 0.8. For each state, lateral views of the left and right hemispheres, together with complementary superior (top-down) and inferior (bottom-up) views are shown. The color bar indicates correlation values.

**Fig. 3. Group differences in the temporal dynamics of brain states between nasal and oral breathing.** (a) Fractional occupancy: oral breathing shows significantly higher occupancy of state 3 (p-FDR = 0.03). (b) Lifetime: nasal breathing is associated with significantly longer persistence of state 2 (p-FDR = 0.03). (c) Switching rate: oral breathing significantly increases the switching rate across states (p-FDR = 0.002). Statistical significance of condition differences was assessed using paired permutation tests (100,000 iterations). Error bars indicate the standard error of the mean (SEM). *$p\text{-FDR} < 0.05$, **$p < 0.01$. All plots were generated using MATLAB (The MathWorks Inc., USA).

**Fig. 4. Group differences and significance of transition probability matrices (TPMs) between nasal and oral breathing.** (a) Difference in transition probability matrices (nasal − oral) across all state transitions. Red indicates a higher transition probability under nasal breathing, whereas blue indicates a higher probability under oral breathing. (b) Statistical significance of condition differences tested using paired permutation tests (100,000 iterations) with FDR correction. Numbers denote p-FDR values; the transition from state 2 to state 3 is significantly higher during oral breathing (*$p\text{-FDR} = 0.022$). All matrices were generated using MATLAB (The MathWorks Inc., USA).

**Fig. 5. Markov chain directed graphs (excluding self-transitions) of states under nasal and oral breathing.** (a) Nasal breathing: transitions are relatively balanced, with a stronger tendency toward state 2. (b) Oral breathing: the graph shows a pronounced directional bias from state 2 to state 3, with a higher tendency toward state 3 compared to nasal breathing. State node sizes are proportional to the inward transition probability, and edge colors represent transition probability values. All graphs were generated using MATLAB (The MathWorks Inc., USA).

**Fig. 6. Topological properties of HMM-derived states across functional connectivity densities.** (a) Global efficiency: state 2 consistently shows the highest efficiency, followed by state 3, while state 1 exhibits the lowest across densities. (b) Local efficiency: averaged across 116 ROIs for each density, results are similar to global efficiency, with state 2 demonstrating stronger local communication, followed by states 3 and 1. (c) Modularity: states 1 and 3 show the highest modularity, whereas state 2 exhibits the lowest, indicating a more integrated network topology. All plots were generated using MATLAB (The MathWorks Inc., USA).

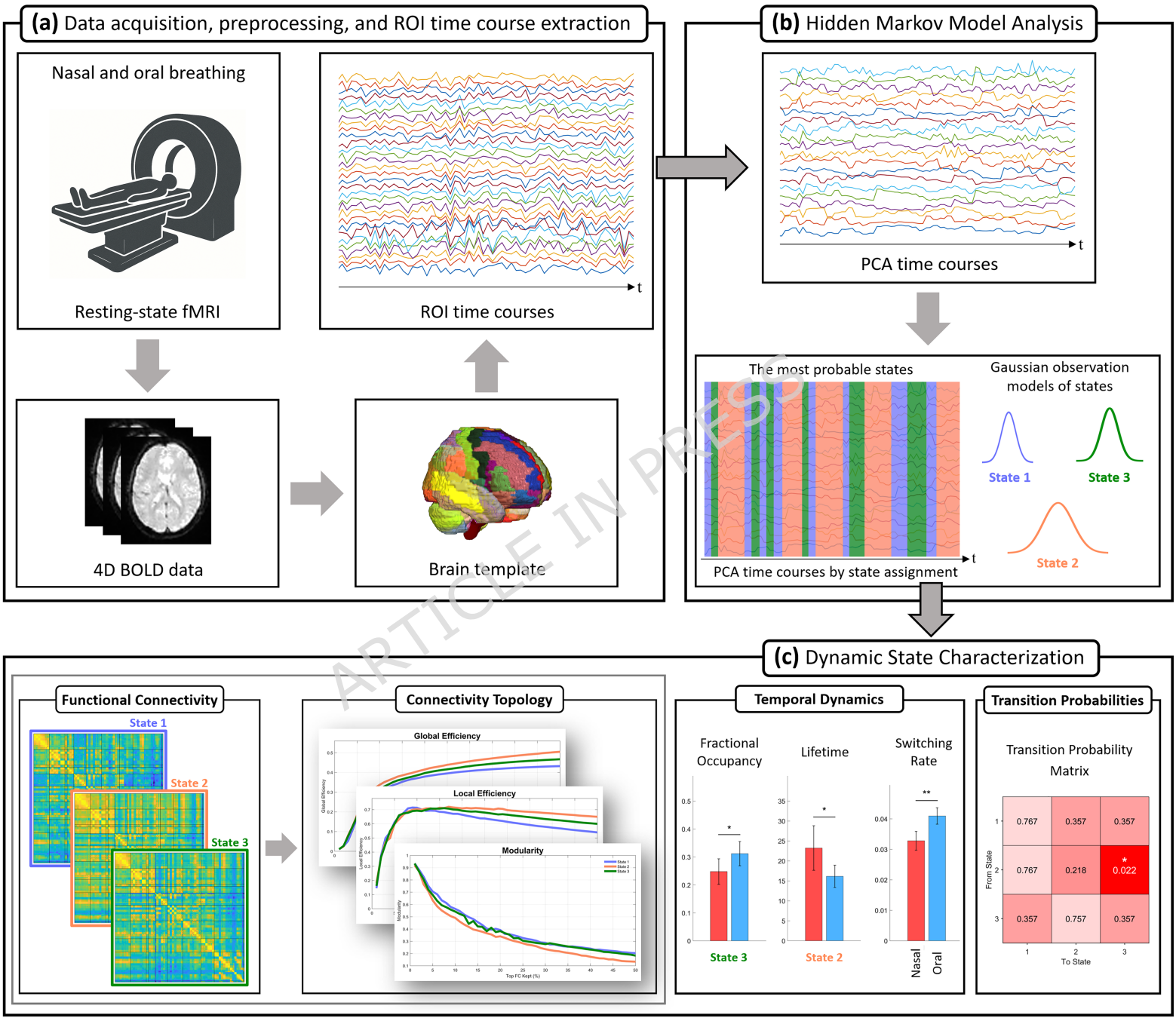

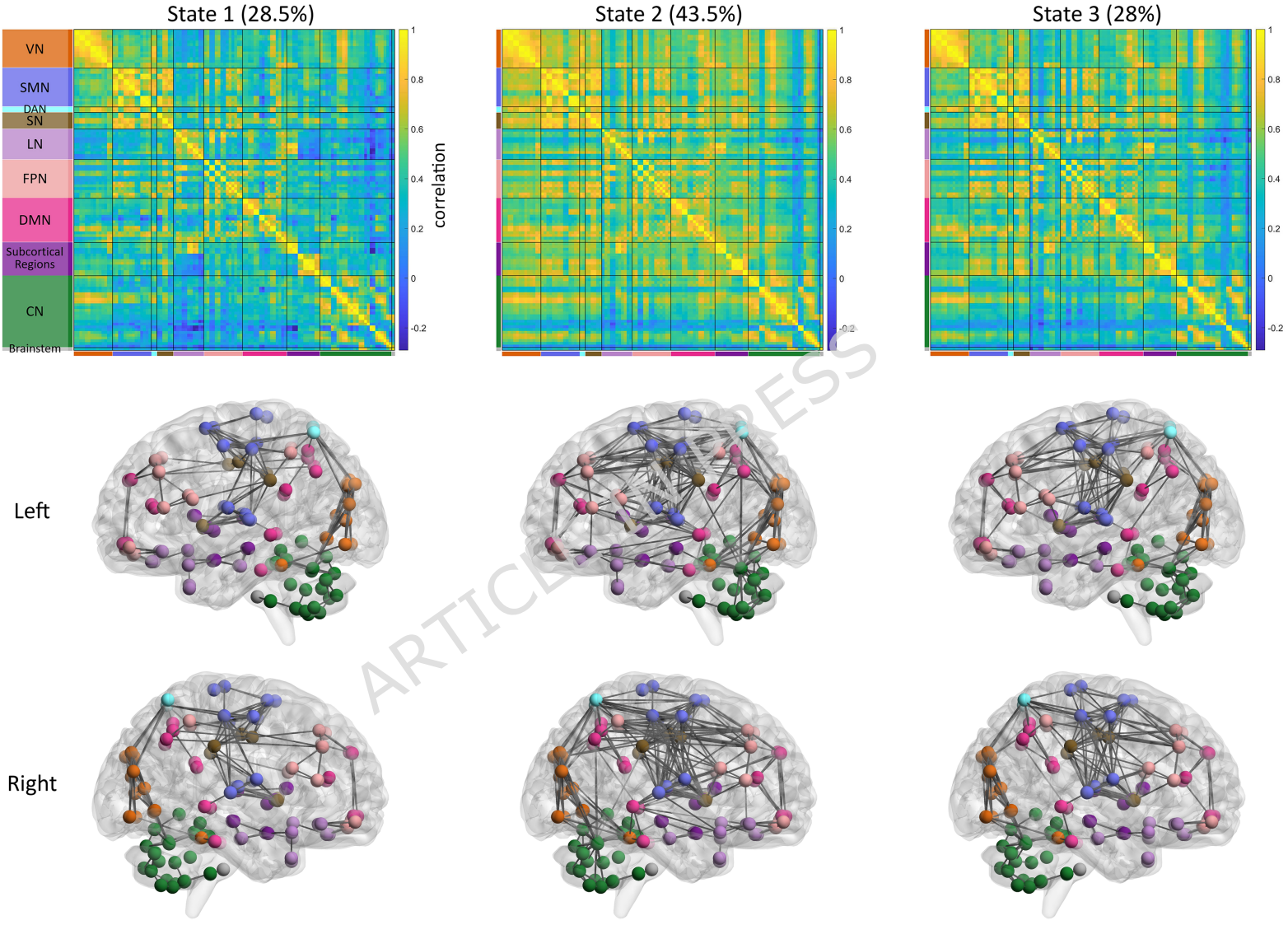

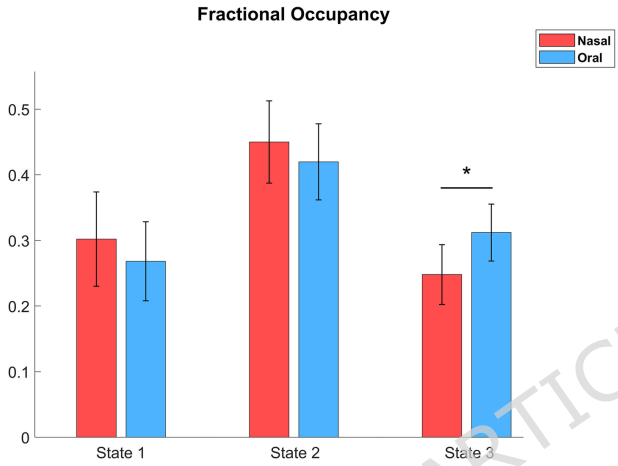


(a)

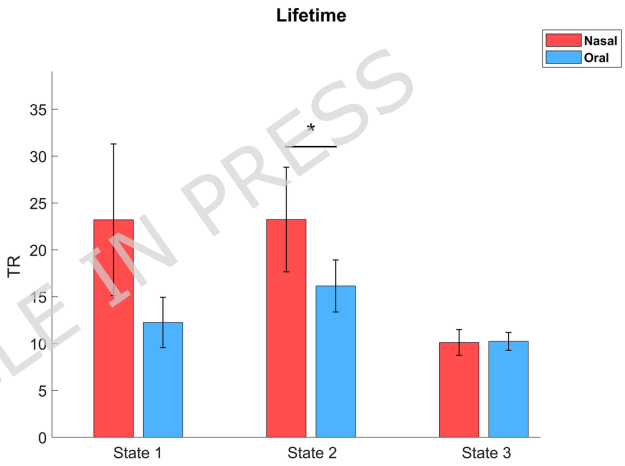


(b)

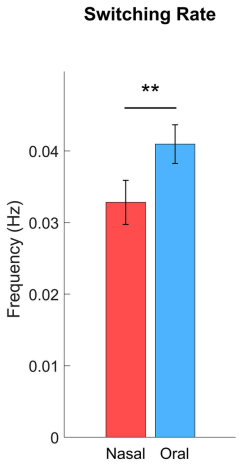


(c)

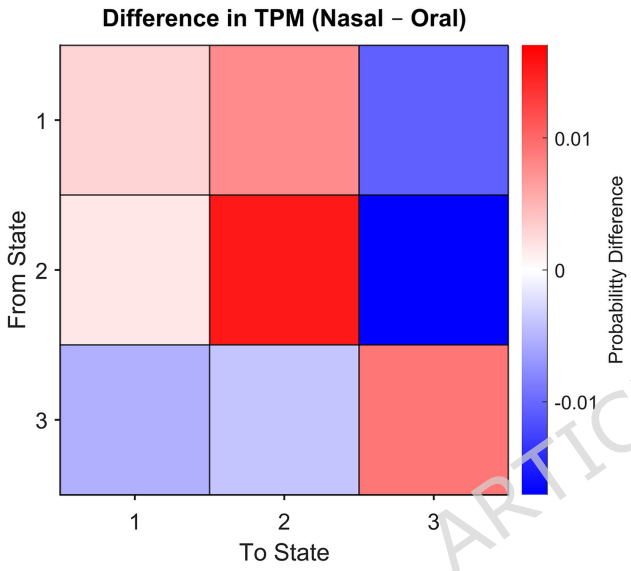


(a)

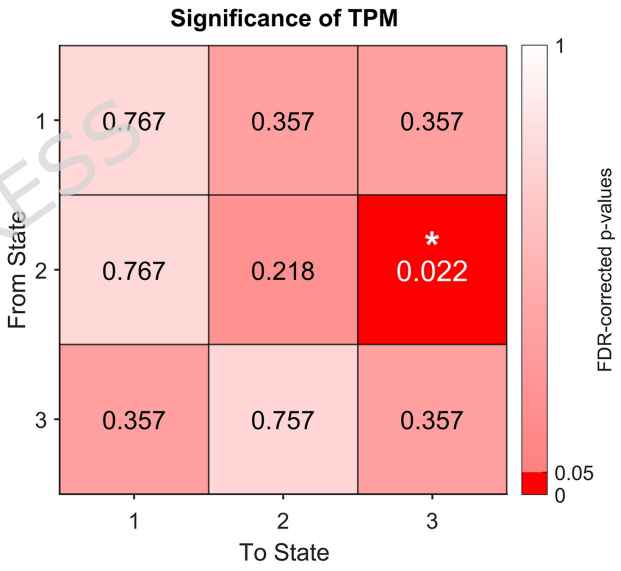


(b)

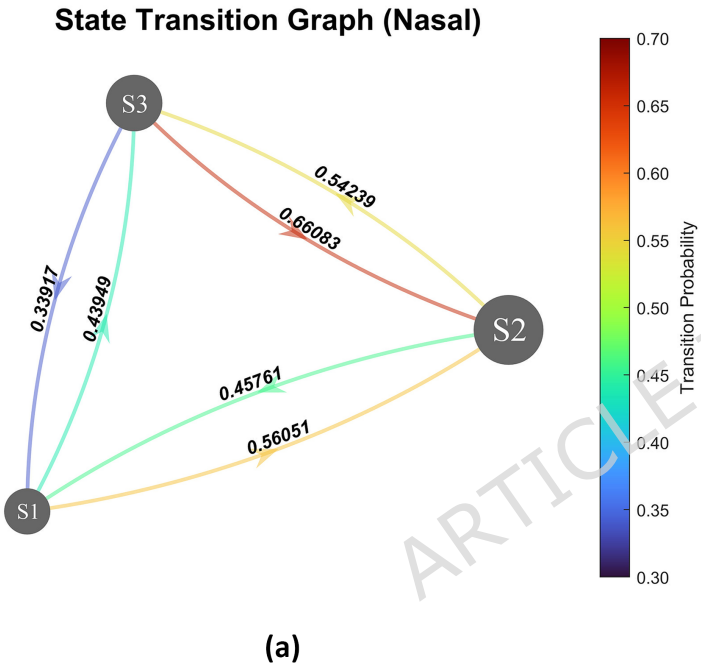


(a)

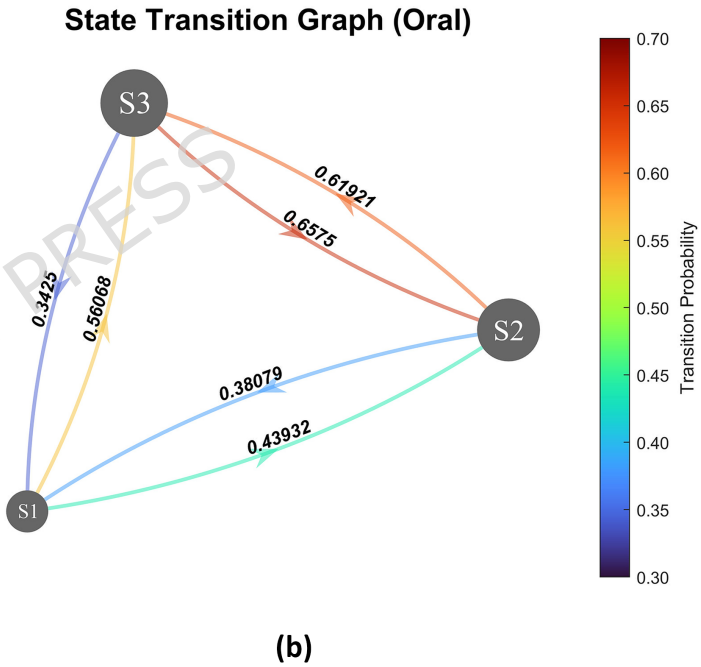


(b)

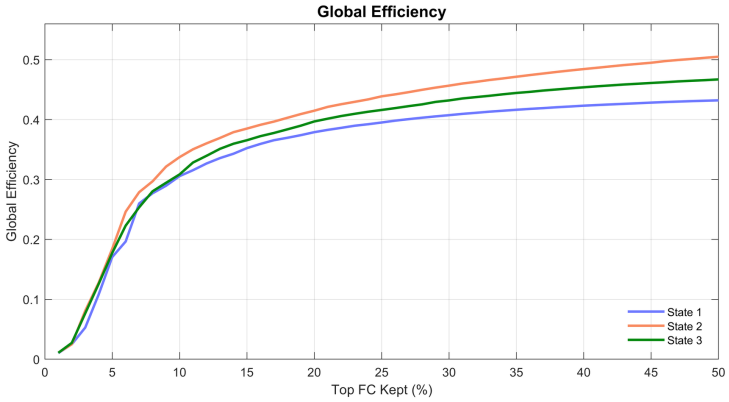


(a)

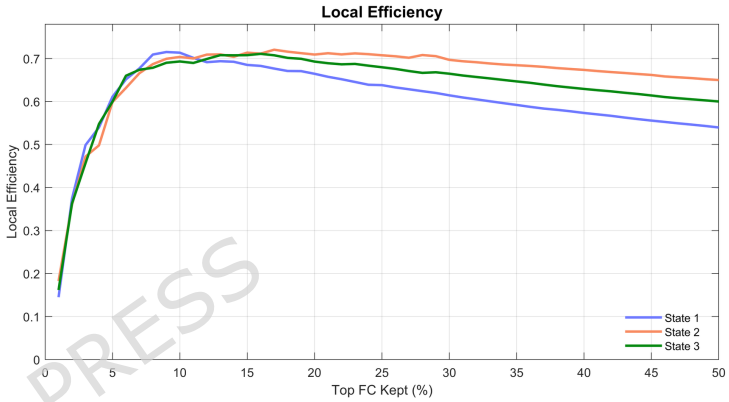


(b)

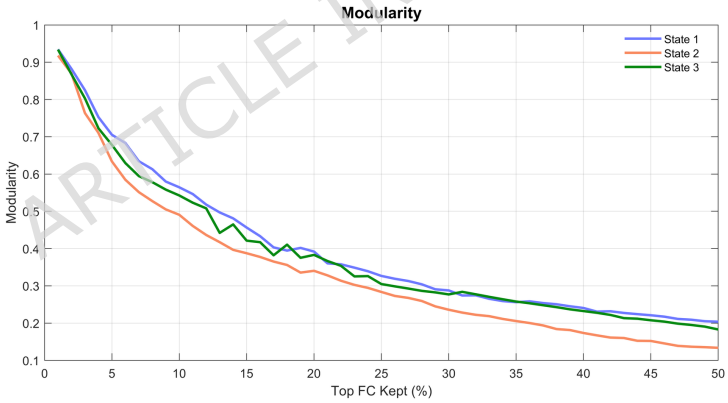


(c)

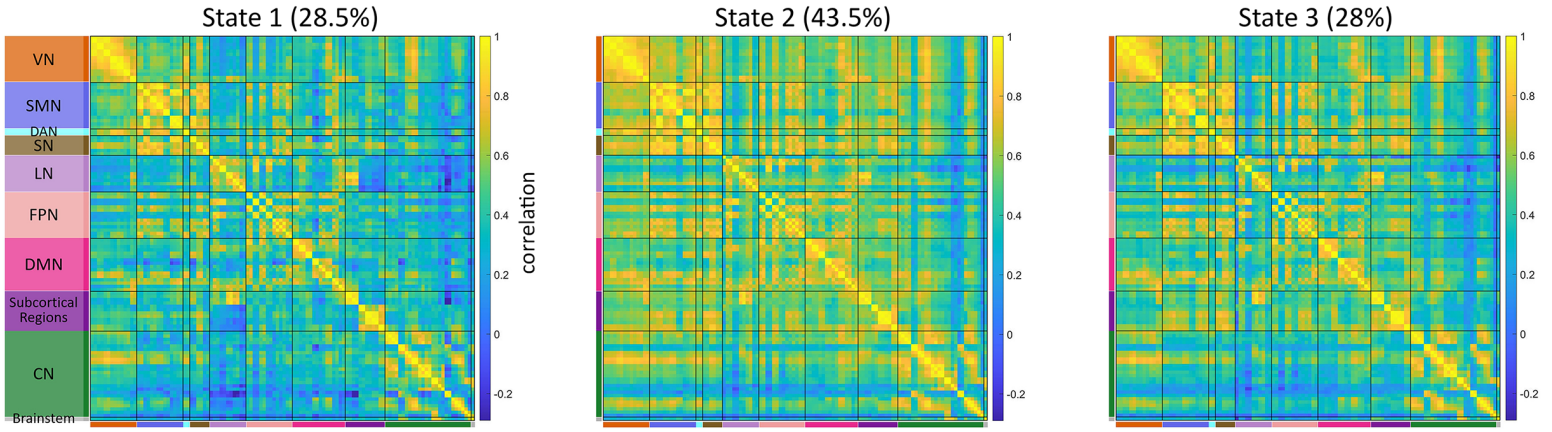


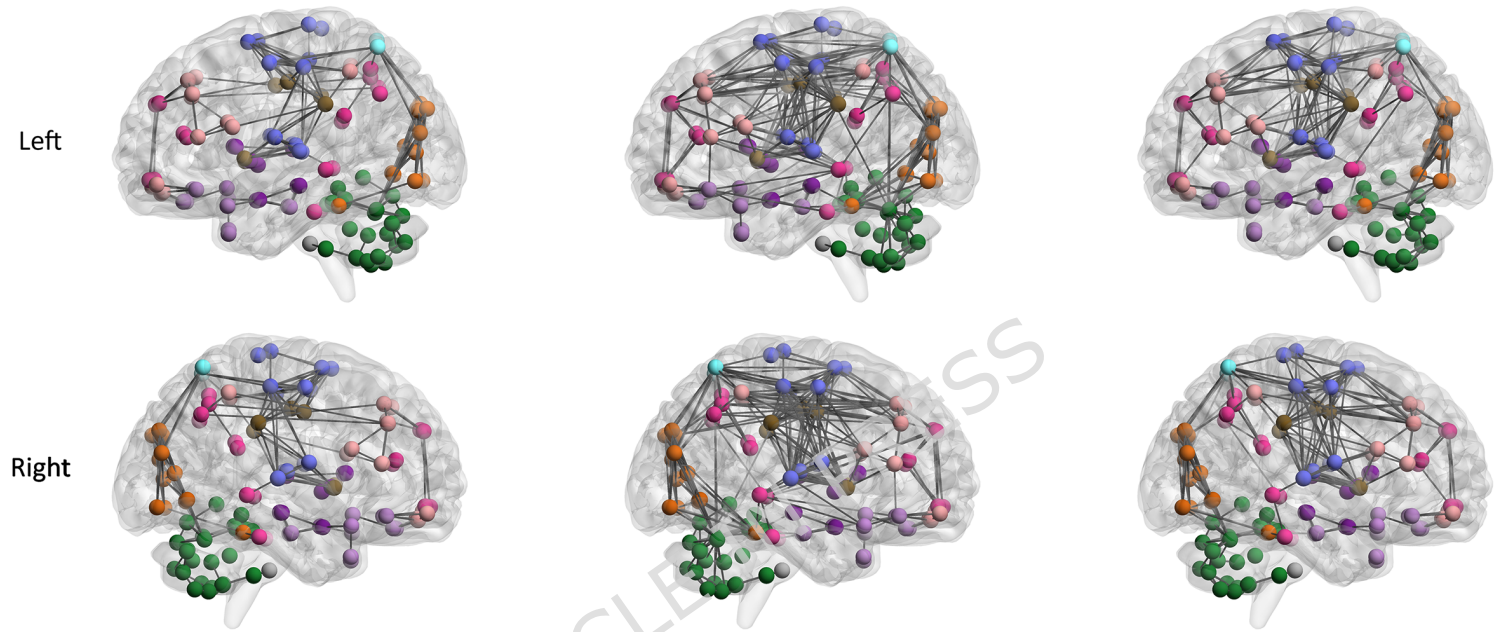


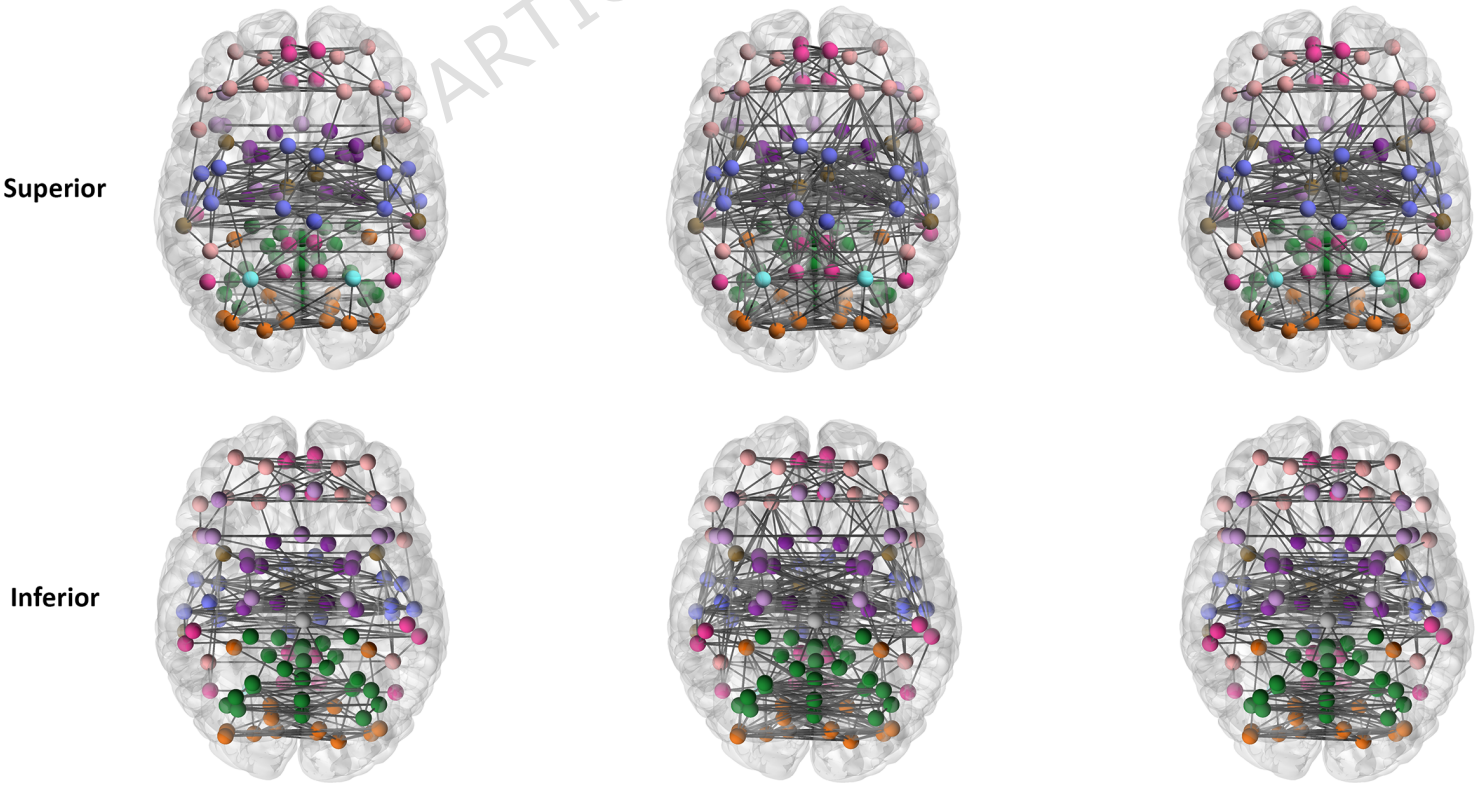


(a) (b) (c)